Chemistry–A European Journal
Research Article
doi.org/10.1002/chem.202203262
Chemistry Europe
European Chemical Societies Publishing
www.chemeurj.org

Neutral, Heteroleptic [Cu(I)$(PPh_3)_2$(4*H*-imidazolato)] Complexes: Ligand Exchange Reactivity, Redox Properties, Excited-State Dynamics

Bianca Seidler[+],[a, b] Jens H. Tran[+],[a] Luise Thomisch,[a] Nikita Vashistha,[a] Helmar Görls,[e] Phil Liebing,[e] Martin Schulz,*[a, b] and Benjamin Dietzek-Ivanšić*[a, b, c, d]

Abstract: Cu(I) 4*H*-imidazolate complexes are rare examples of Cu(I) complexes with chelating anionic ligands and are potent photosensitizers with unique absorption and photoredox properties. In this contribution, five novel heteroleptic Cu(I) complexes with monodentate triphenylphosphine coligands are investigated. As a consequence of the anionic 4*H*-imidazolate ligand and in contrast to comparable complexes with neutral ligands, these complexes are more stable than their homoleptic bis(4*H*-imidazolato)Cu(I) congeners. Here, the ligand exchange reactivity was studied by ^{31}P-,^{19}F-, and variable temperature NMR and the ground state structural and electronic properties by X-ray diffraction, absorption spectroscopy, and cyclic voltammetry. The excited-state dynamics were investigated by femto- and nanosecond transient absorption spectroscopy. The observed differences, with respect to chelating bisphosphine bearing congeners, are often due to the increased geometric flexibility of the triphenylphosphines. These observations render the investigated complexes interesting candidates for photo(redox)reactions not accessible with chelating bisphosphine ligands.

Introduction

The conversion of solar energy into chemical energy by using molecules or materials based on earth-abundant metals constitutes a prime research path toward a sustainable future.[1–9] In this context, artificial photosynthesis, that is, following inspirations from nature in designing photocatalytically active systems to generate sustainable fuels, has matured.[3,4,8,9] Still, one of the major challenges, aside from designing highly active molecular catalysts, is the synthesis of noble-metal free molecular photosensitizers with a broad and intense absorption range in the visible region, a reversible electrochemical behavior, long lifetimes of the excited-state and a high (photo)stability under the reaction conditions.[2,3,5,10,11] A representative of this class of functional molecular components for artificial photosynthesis are Cu(I) complexes, which have a simple and low-cost synthesis as well as the aforementioned requirements.[1,2,4–7,10,12,13]

Since the seminal report of McMillin, Walton and coworkers in 2002[14] chelating phosphine ligands, such as xantphos or POP (=DPEPhos) have become very popular among heteroleptic Cu(I) complexes. The usage of chelating phosphines instead of monodentate triphenylphosphine was motivated by significant exciplex quenching for [Cu$(PPh_3)_2$(NN)]$^+$ complexes (NN for example being 1,10-phenanthroline or 2,9-dimethyl-1,10-phenanthroline) in methanol[15,16] and a hard control of the speciation, that is, the coordination of the counter anion or formation of the homoleptic complexes.[15–19] It was observed that coordination chemistry and excited state properties depend on the interplay of steric and electronic ligand properties. For instance [Cu$(PPh_3)_2$(2,9-dimethylphenanthroline)]$^+$ is more prone to undergo PPh_3 ligand dissociation than [Cu$(PPh_3)_2$(phenanthroline)]$^+$ due to inter-ligand steric repulsion but exhibits appreciable emission from a charge transfer state as a result of the crowded coordination sphere (avoidance of exciplex quenching).[16,20] Additionally, cationic [Cu$(PPh_3)_2$(NN)]$^+$ complexes were studied towards their antiproliferative effect

[a] *B. Seidler,[+] J. H. Tran,[+] L. Thomisch, N. Vashistha, M. Schulz, B. Dietzek-Ivanšić*
Institute of Physical Chemistry
Friedrich Schiller University Jena
Helmholtzweg 4, 07743 Jena (Germany)
E-mail: martin.schulz.1@uni-jena.de
benjamin-dietzek@leibniz-ipht.de
[b] *B. Seidler,[+] M. Schulz, B. Dietzek-Ivanšić*
Leibniz Institute of Photonic Technology Jena (Leibniz-IPHT)
Albert-Einstein-Str. 9, 07745 Jena (Germany)
[c] *B. Dietzek-Ivanšić*
Abbe Center of Photonics (ACP)
Albert-Einstein-Str. 6, 07745 Jena (Germany)
[d] *B. Dietzek-Ivanšić*
Center for Energy and Environmental Chemistry Jena (CEEC-Jena)
Friedrich Schiller University Jena
Philosophenweg 7a, 07743 Jena (Germany)
[e] *H. Görls, P. Liebing*
Institute of Inorganic and Analytical Chemistry
Friedrich Schiller University Jena
Humboldtstraße 8, 07743 Jena (Germany)
[+] *These authors contributed equally to this work.*
Supporting information for this article is available on the WWW under https://doi.org/10.1002/chem.202203262

and DNA binding[21], catalytic coupling of aromatic carboxylates with aryl halides[22], or CO_2 insertion into C–H bonds.[23]

We have introduced [Cu(xantphos)(4*H*-imidazolato)] ([Cu(xantphos)(Im)]) complexes as a new class of heteroleptic Cu(I) complexes, which combine a broad and intense absorption in the visible range with sufficiently long excited-state lifetimes (up to 130 ns).[8,24–27] Light-driven two-electron charge accumulation in these complexes was realized in the presence of a sacrificial electron donor. The charges accumulated in the complexes upon photochemical reduction could be stored in the complexes for more than 14 h.[24] In a dark reaction, the charges could then be extracted upon adding suitable acceptors, hence, effectively separating light and dark reaction. This finding paves the way to a fully molecular system for on-demand-solar-driven reductive catalysis.[24,28] An important feature of these Cu(I)4*H*-imidazolato complexes is the anionic nature of the ligand. Thus, in addition to the dative binding of the 4*H*-imidazolate ligand to the Cu(I) center, Coulomb-interactions are anticipated. Furthermore, the torsional flexibility of the *N*-aryl moieties may allow steric adaption to bulky co-ligands, such as PPh_3. In view of the potential (photo)catalytic application of this complex class, we were interested in the synthesis and complex stability, ground-state absorption and electrochemistry as well as in the excited-state relaxation dynamics of the neutral [Cu$(PPh_3)_2$(4*H*-imidazolato)] complexes ([Cu$(PPh_3)_2$Im], see Scheme 1). In this contribution, we discuss the synthetic route, NMR experiments as well as absorption and electrochemistry. Finally, transient absorption spectroscopy sheds light on the excited-state dynamics using two different excitation wavelengths and with respect to varying electronic and steric properties of the 4*H*-imidazole ligand.

Results and Discussion

Synthesis

The title compounds were synthesized following an adaption of a previously reported route,[26] using Amberlyst A21 as a solid-state base for the deprotonation of the bidentate 4*H*-imidazole (HIm) ligands in dichloromethane solution (see Scheme 1). To this solution, a mixture of PPh_3 and [Cu(acetonitrilo)$_4$]PF_6 in acetonitrile was added to receive the title compounds, as red crystals after filtration and crystallization. For the purpose of comparison, the xantphos analogue of **Cu–CF$_3$** ([Cu(xantphos)Im–CF_3]) was prepared, following the previously published procedure.[26]

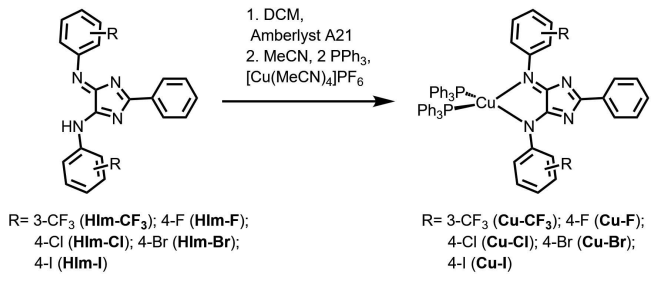

R= 3-CF_3 (**HIm-CF$_3$**); 4-F (**HIm-F**); 4-Cl (**HIm-Cl**); 4-Br (**HIm-Br**); 4-I (**HIm-I**)

R= 3-CF_3 (**Cu-CF$_3$**); 4-F (**Cu-F**); 4-Cl (**Cu-Cl**); 4-Br (**Cu-Br**); 4-I (**Cu-I**)

Scheme 1. General reaction scheme towards heteroleptic Cu(I) complexes **Cu–CF$_3$**, **Cu–F**, **Cu–Cl**, **Cu–Br** and **Cu–I**.

Structural characterization

The identity of the compounds was verified by one- and two-dimensional NMR methods, mass spectrometry, CHN-elemental analysis, and X-Ray diffraction (for further information see Supporting Information Chapter 6). The ^{1}H NMR shows only one set for the *N*-aryl protons suggesting a symmetric molecule. The experimental mass spectra reveal two PPh_3 ligands, one 4*H*-imidazolate ligand and one Cu per molecule. The measured isotope pattern agrees with the calculated pattern and confirms the identity of the complexes. CHN-elemental analysis affirms the homogeneity of the samples. From **Cu–CF$_3$**, **Cu–Cl**, and [Cu(xantphos)Im–CF_3] single crystals were obtained with qualities sufficient for single-crystal X-Ray structure determination (Figure 1 depicts the molecular structure of **Cu–CF$_3$** as an example); the results reflect the assumed structures (Scheme 1). The structural parameters of the [Cu(xantphos)Im–CF_3] complex, which crystallized in the monoclinic space group $P2_1/c$, are consistent with previously published data from [Cu(xantphos)Im] complexes.[24–26]. The Cu(I) center adopts a distorted tetrahedral coordination sphere and the Cu–N and Cu–P bond lengths are in the range of previously reported [Cu(xantphos)Im] complexes.[24–26] For **Cu–CF$_3$** the Cu–N and Cu–P bonds are similar to the xantphos analogue [Cu(xantphos)Im–CF_3]. The N–Cu–N bite angles are also in the range of the [Cu(xantphos)Im] analogues and are essentially the same for **Cu–CF$_3$** and **Cu–Cl** with ca. 82°. The P–Cu–P bite angles are larger for the [Cu$(PPh_3)_2$(Im)] complexes (120° and 128° for **Cu–CF$_3$** and **Cu–Cl**, respectively) than for [Cu(xantphos)Im–CF_3] (116°) as a consequence of the monodentate ligation of PPh_3, in contrast to the chelating xantphos ligand. The higher conformational flexibility of the PPh_3 ligands lets the

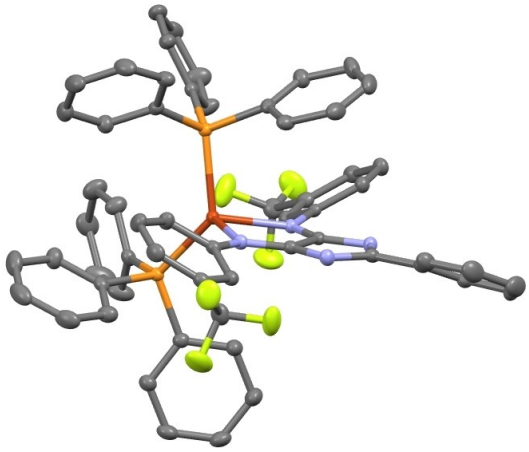

Figure 1. Molecular structure of **Cu–CF$_3$** determined by single-crystal X-ray diffraction. Ellipsoids are drawn at the 50% probability level and H atoms and solvent molecules have been omitted for the sake of clarity.

Cu(I) adopt a less distorted tetrahedral coordination sphere, perceptible by the larger dihedral angle between the P–Cu–P and N–Cu–N planes in the [Cu(PPh_3)$_2$Im] complexes (**Cu–CF$_3$**: 86°; **Cu–Cl**: 88°; [Cu(xantphos)Im–CF_3]: 83°), see Table S3.

Ligand exchange reactions in solution

Fluxional behavior of heteroleptic [Cu(PPh_3)$_2$(NN)]$^+$ complexes were reported previously as already discussed above.[16,29] It is important to note that in the case of Cu(I) 4*H*-imidazolate complexes, ligand disproportionation would yield complex ions due to the anionic nature of the Im$^-$ ligand. This is in contrast to [Cu(PPh_3)$_2$(NN)]$^+$ complexes with neutral ligands and thus a different ligand exchange reactivity can be expected. The ligand exchange reactivity was studied by NMR and UV-Vis absorption in non-coordinating dichloromethane and coordinating acetonitrile. ^{1}H, ^{31}P, and ^{19}F NMR chemical shifts as well as the electronic transitions are sensitive to alterations of the coordination sphere by virtue of an altered electron density on the 4*H*-imidazolate ligand. To exclude interference from trace water, all NMR and UV-Vis absorption experiments were conducted under a nitrogen atmosphere with degassed, anhydrous solvents, if not stated otherwise.

NMR spectra of the title compounds in CD_2Cl_2 or CD_3CN show no indication for the formation of homoleptic [Cu(Im)$_2$]$^-$, [Cu(Solv)$_2$Im] or unbound PPh_3. Additionally, neither an Im$^-$ ligand exchange reaction is observed for a 1:1 mixture of **Cu–CF$_3$** and **Cu–F** dissolved in CD_2Cl_2, nor the formation of the respective homoleptic or heteroleptic cuprates (see Supporting Information Figure S1).

Interestingly, however, the ^{31}P NMR of the 1:1 mixture of **Cu–CF$_3$** and **Cu–F** dissolved in CD_2Cl_2 shows one broad signal at $\delta = -0.12$ ppm, which lies between the resonances of the respective pure compounds ($\delta = 0.16$ ppm, **Cu–CF$_3$**; $\delta = -0.36$ ppm, **Cu–F**; Figure S2). This ^{31}P resonance does not shift or change at temperatures between 253 to 297 K. In contrast, the ^{19}F NMR spectra, show the two resonances of the pure compounds ($\delta = -62.55$ ppm, **Cu–CF$_3$**; $\delta = -119.13$ ppm, **Cu–F**; Figure S3). These observations indicate that Im$^-$ ligand exchange equilibria are disfavored in CD_2Cl_2 but suggest a dynamic exchange of the PPh_3 ligand. The absence of Im$^-$ ligand exchange reactions and the stability of the title complexes over their homoleptic congeners ([Cu(Im)$_2$]$^-$) is in contrast to [Cu(PPh_3)$_2$(NN)]$^+$-type complexes and attributed to the anionic nature of Im$^-$.

The PPh_3 ligand exchange reactions were further investigated by NMR spectroscopy upon the addition of PPh_3 to the heteroleptic **Cu–CF$_3$** and homoleptic [Cu(Im–CF_3)$_2$]$^-$ N(butyl)$_4^+$ in CD_2Cl_2 (Figure S7). When 1 equiv. of PPh_3 was added to **Cu–CF$_3$** an averaged ^{31}P NMR resonance was observed at $\delta = -1.88$ ppm and 297 K. Cooling the solution to 233 K furnished a split into two singlets, which are assigned to **Cu–CF$_3$** ($\delta \sim 1$ ppm) and unbound PPh_3 ($\delta \sim -5$ ppm), in accord with authentic samples (Figure 2). The NMR data do not indicate the formation of other species than those initially added. The integral ratio of [Cu(PPh_3)$_2$Im–CF_3] : PPh_3 equals 2:1.2 (determined from ^{31}P NMR at 233 K) The temperature dependency unravels a fast dynamic exchange of coordinated and uncoordinated PPh_3, which results in an averaged signal of $\delta = -1.88$ ppm at 298 K. When the solution is cooled down the exchange process is slowed down so that both the **Cu–CF$_3$** species and the uncoordinated PPh_3 are observed on the NMR time scale.

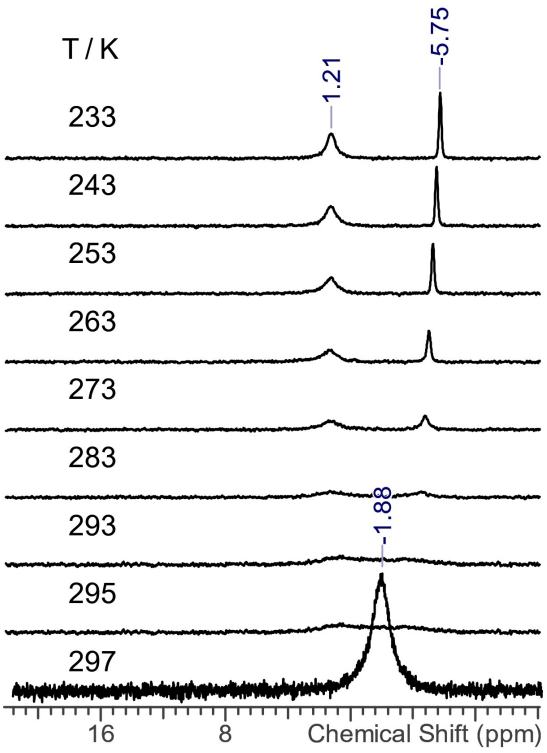

Figure 2. ^{31}P NMR (162 MHz, CD_2Cl_2) of **Cu–CF$_3$** and 1 eq. of PPh_3 at different temperatures.

Addition of 1 equiv. of PPh_3 to a solution of the homoleptic [Cu(Im–CF_3)$_2$]$^-$ N(butyl)$_4^+$ led to a color change from deep blue to red, indicating the formation of the heteroleptic **Cu–CF$_3$** (Scheme 2). At 293 K, the ^{31}P NMR shows one broad signal at $\delta = 0.71$ ppm, which splits into two signals at $\delta = 1.3$ ppm and $\delta = -4.7$ ppm at 273 K. The signal at $\delta = 1.3$ ppm is assigned to **Cu–CF$_3$** and the signal at $\delta = -4.7$ ppm is assigned to unbound PPh_3 (Figure S8). Moreover, when an additional equivalent of PPh_3 is added two broad but distinct signals are visible, which merge with the addition of a third equivalent of PPh_3 (Figure S9). In the respective ^{19}F NMR, three resonances are observed (Figure S10). A signal with high intensity at $\delta = -62.7$ ppm and two less intensive signals at $\delta = -62.5$ ppm/-62.6 ppm. The signal at -62.7 ppm is assigned to [Cu(Im–CF_3)$_2$]$^-$ and the signals at -62.5/-62.6 ppm are assigned to Im–CF_3^-/**Cu–CF$_3$** respectively. The molar ratio, determined from ^{19}F NMR is: Im–CF_3:**Cu–CF$_3$**:[Cu(Im–CF_3)$_2$] = 0.40:0.40:1 (compare with Figure S9 and S10). The formation of the heteroleptic **Cu–CF$_3$** complex is also observed via UV-Vis spectroscopy in dichloromethane and acetonitrile and leads to the shift and decrease of the visible absorption band with an increasing

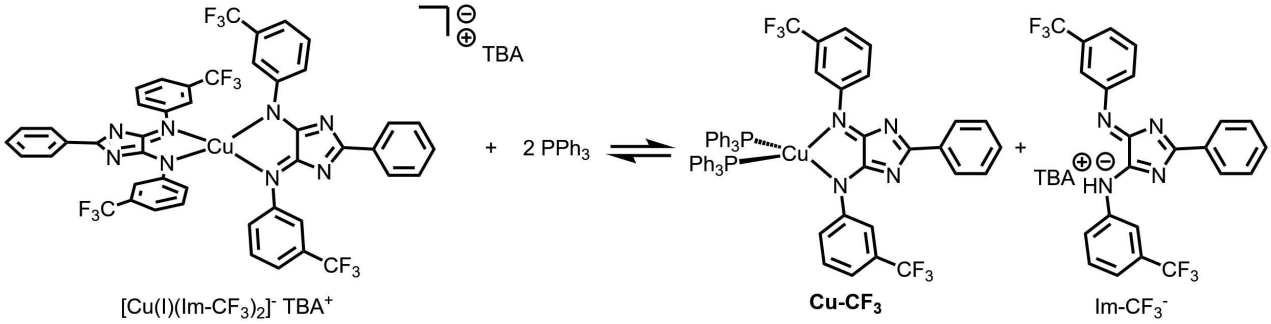

Scheme 2. Ligand exchange equilibrium in CD_2Cl_2 of the homoleptic $[Cu(Im{-}CF_3)_2]^-$ $N(butyl)_4^+$[30] with 1 equiv. of PPh_3 under formation of **Cu**–$\mathbf{CF_3}$.

amount of added PPh_3 (see Supporting Information Figure S11 and S12). The absorption maximum shifts from 550 nm to 530 nm and the typical red-to-NIR bands of $[Cu(Im{-}CF_3)_2]^-$ $N(butyl)_4^+$ decrease.

To investigate possible light-dependent PPh_3 exchange processes, NMR and UV-Vis investigations were performed under illumination conditions. In the first experiment, *in situ* illumination of **Cu**–$\mathbf{CF_3}$ was carried out in CD_2Cl_2 under atmospheric conditions in a coaxial NMR tube, with the light source in the inner tube (455 nm fiber LED, for details, see Supporting Information Chapter 1.2.4). In a second experiment, a mixture of **Cu**–$\mathbf{CF_3}$ and **Cu**–**F** in CD_2Cl_2 in an airtight NMR tube was irradiated *ex situ* with a white light LED and subsequently measured. In all cases, the ^{31}P NMR did not indicate ligand exchange reactions since the signal is virtually unchanged after irradiation (see Supporting Information Figure S5).

Photoreduction with a sacrificial donor

Cu(I) 4*H*-imidazolate complexes undergo two-electron photoreduction in the presence of a sacrificial electron donor (e.g., *N*,*N*-dimethyltoluidin, DMT), yielding the colorless Cu(I) 1*H*-imidazolate complex.[24] The Cu(I) 1*H*-imidazolate complex is stable under anaerobic conditions and can react with an electron acceptor, such as oxygen or methyl viologen in a dark reaction.[24]

The photoreduction of the title compounds was investigated with the complexes **Cu**–$\mathbf{CF_3}$ and **Cu**–**F** in acetonitrile in the presence of excess DMT. The reaction mixture was irradiated with a white light LED (see Supporting Information Figure S13–14 for further details) until no further decrease of the visible absorption band was detected (~150 h; photoreduction yield: **Cu**–$\mathbf{CF_3}$ 91%; **Cu**–**F**: 86%). As a typical test[24] for the reversibility of the photoreduction, the solution was allowed to react with air (see Supporting Information Figure S14 for further details). The formation of the initial Cu(I) 4*H*-imidazolate complex is followed by the recovery of the visible absorption band to the initial absorbance. For **Cu**–$\mathbf{CF_3}$ about 75% of the absorption was recovered. However, the reoxidation with air does not yield entirely identical absorption spectra compared to the initial spectrum, which is presumably due to partial degradation. For **Cu**–**F** the spectral shape changes significantly during reoxidation indicating degradation under the applied conditions. Additionally, Stern-Volmer quenching experiments were conducted in the presence of excess DMT. **Cu**–**F** and **Cu**–**I** were chosen for these experiments owing to their comparatively long excited state lifetimes (see below). As observed before,[24] even a 1000-fold DMT excess does not change the nanosecond lifetime and the reasons yet remain elusive. The estimated quenching rates between DMT and the complex show, that the bimolecular quenching is not limited by diffusion (see Supporting Information Chapter 4.1).

Ground-state absorption properties

The absorption spectra of the heteroleptic Cu(I) complexes dissolved in acetonitrile are shown in Figure 3. For all three heteroleptic Cu(I) complexes an intense and sharp peak appears

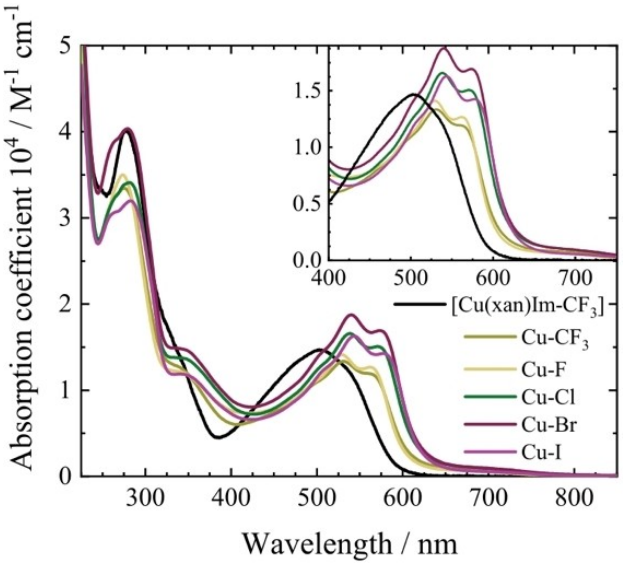

Figure 3. Absorption coefficients of $[Cu(xantphos)Im{-}CF_3]$ (black), **Cu**–$\mathbf{CF_3}$ (olive), **Cu**–**F** (yellow), **Cu**–**Cl** (green), **Cu**–**Br** (brown) and **Cu**–**I** (violet) were measured in acetonitrile.

at 275 nm, which is assigned to PPh_3-based π–π* transitions.[12,25,31] A shoulder at about 350 nm is assigned to intra-ligand π–π* transitions of the 4*H*-imidazolate ligand.[11,25,31] Broad double bands occur from 450 to 600 nm with slightly red-shifted maxima for **Cu–Cl**, **Cu–Br**, **Cu–I** (~540 nm) compared to **Cu–CF_3** and **Cu–F** (~530 nm). Based on TD-DFT calculations, the broad double band is composed of four charge transfer transitions that have mixed character with strong metal and ligand contributions to the donor states (see Supporting Information Chapter 6). The molecular absorption coefficients in the visible range increase in the order **Cu–CF_3** < **Cu–F** < **Cu–I** ~ **Cu–Cl** < **Cu–Br**.

In comparison, the absorption spectrum of [Cu(xantphos)Im–CF_3] has an intense band at 275 nm and a shoulder at 340 nm, which are assigned to xantphos based and 4*H*-imidazolate transitions, respectively.[6,26,31] The broad visible band from 390 to 600 nm is composed of four transitions of metal-to-ligand and intra-ligand charge transfer character and appears blue-shifted with respect to the title complexes.[25,27]

In dichloromethane or acetonitrile solution, the title complexes show a weak NIR absorption at 700 nm even under inert and atmospheric conditions. This absorption at 700 nm is not reproduced by the TD-DFT calculations and the origin of this band so far remains unclear (see Supporting Information Figure S37).

Ground-state redox properties

The electrochemical properties of the title compounds were investigated using cyclic voltammetry. Voltammograms were generated using a glassy carbon working electrode, Ag rod pseudo-reference electrode and Pt rod counter electrode in acetonitrile/$TBAPF_6$. All redox potentials are referenced against ferrocene. For **Cu–CF_3**, **Cu–F**, **Cu–Cl** and **Cu–Br**, three cathodic and two anodic waves are observed (see Supporting Information Chapter 3). For **Cu–I** four cathodic and two anodic waves occur. The first cathodic wave is reversible for all the complexes as indicated by the peak-to-peak separation of 60–80 mV. It is assigned to a 4*H*-imidazolate reduction based on previous publications investigating the xantphos congeners.[24–26] Also the second, irreversible cathodic wave is assigned to a 4*H*-imidazolate reduction, in good agreement with the xantphos congeners. The peak current of the backward scan is significantly lower than the forward scan, when measured to the lowest possible cathodic potential in acetonitrile, due to associated chemical reactions. Additional waves occur in the backward scan, which are decreased by measuring in smaller potential windows. These reoxidation waves (~−1 V *vs.* Fc/Fc^+) are almost completely prevented when only the first cathodic wave is scanned.

For [Cu(xantphos)Im–CF_3] two reduction waves occur (see Supporting Information Figure S17). The first reduction wave is reversible, while the second is irreversible, the reductions occur at similar potentials as the first two reductions of the [Cu(PPh_3)$_2$Im] complexes (see Table 1). Similar to the [Cu(PPh_3)$_2$Im] complexes, no additional waves in the backward scan appear when measuring only the first reduction wave. A third reduction wave is observed for [Cu(PPh_3)$_2$Im] (four reduction waves for **Cu–I**) but not for [Cu(xantphos)Im–CF_3]. A reduction of Cu(I) to Cu(0) as well as a reduction of the PPh_3 ligand are excluded. Cyclic voltammograms of pure PPh_3 do not indicate any reduction processes (see Supporting Information Figure S23). Although the third (and fourth) reduction events cannot be assigned, it is likely, that the electrochemical process is coupled to a chemical reaction, such as dehalogenation.[32] Interestingly, the PPh_3 ligand seems to favor this chemical step as **Cu–CF_3** has a third reduction wave, while the xantphos analogue does not. The introduction of xantphos as a ligand seems to improve the electrochemical stability of the resulting complexes.[12,16,33–38]

The first and second reduction potentials are similar for **Cu–CF_3** and **Cu–F** (~−1.6 V and −2.1 V *vs.* Fc/Fc^+) and for **Cu–Cl**, **Cu–Br** and **Cu–I** (−1.5 V and −2.0 V *vs.* Fc/Fc^+). In contrast to the homoleptic TBA[Cu(Im)$_2$] complexes, where a trend depending on the electronic effect of the substitution pattern was observed.[39] No clear influence of the substituent on the electrochemical reduction of the title compounds is found. The second reduction shows a similar trend as the first, although the difference between the second reduction potential of **Cu–CF_3** and **Cu–F** is slightly larger, 70 mV instead of 30 mV, for the other complexes (the second reduction potential of **Cu–I** is not taken into account since it could not be assigned unambiguously to a 4*H*-imidazolate-based reduction). The first reduction of **Cu–CF_3** occurs at about 70 mV higher potential than for [Cu(xantphos)Im–CF_3] indicating a slightly higher electron density on the 4*H*-imidazolate for **Cu–CF_3**.

In the anodic scan, two irreversible waves are observed between +0.8 to +0.9 V, and +1.3 to +1.4 V *vs.* Fc/Fc^+, respectively. The first oxidation is assigned to the oxidation of Cu(I), in agreement with previous reports and [Cu-

Table 1. Summary of redox potential recorded by cyclic voltammetry in acetonitrile *vs.* Fc/Fc^+. Values for the half step potentials or peak potentials in V are given for a scan rate of 1 V/s, peak-to-peak separation in mV in parentheses.

Complex	$E_{red,1}$	$E_{red,2}$	$E_{red,3/4}$	$E_{ox,1}$	$E_{ox,2}$
[Cu(xantphos)Im–CF_3]	−1.59 (60)[a]	−2.19 (60)[a]	Not observed	+0.70[b]	+1.09[b]
Cu–CF_3	−1.66 (60)[a]	−2.13 (150)[a]	−2.51 (92)[a]	+0.88[a]	+1.27[b]
Cu–F	−1.63 (70)[a]	−2.06 (170)[a]	−2.53	+0.91[b]	+1.35[b]
Cu–Cl	−1.51 (60)[a]	−2.00 (80)[a]	−2.35	+0.92[b]	+1.36[b]
Cu–Br	−1.52 (60)[a]	−1.98 (60)[a]	−2.36[b]	+0.93[b]	+1.39[b]
Cu–I	−1.51 (79)[a]	−2.04[b]	−2.46/-2.70[b]	+0.92[b]	+1.34[b]

[a] Half-step potential calculated from the anodic and cathodic wave [b] Peak potential determined from the wave in the forward scan.

(xantphos)Im–CF_3].[4,25,26,40] The second irreversible oxidation is assigned to the oxidation of the PPh_3 ligand.[25] This is further supported by the measurement of pure PPh_3 under the same conditions, which gives an irreversible oxidation wave at +0.84 V *vs.* Fc/Fc^+. Due to the electron-withdrawing effect of the Cu(I) the oxidation potential of coordinated PPh_3 is higher than for free PPh_3. For the 4*H*-imidazolates no oxidation was observed.[39]

Excited-state absorption properties

To study the excited-state photophysics, the complexes **Cu–CF_3**, **Cu–F** and **Cu–I** were investigated by transient absorption (TA) spectroscopy exciting in the visible absorption band either at 400 or at 540 nm. Based on the theoretical analysis of the steady-state absorption spectra presented above the visible absorption band transitions are charge transfer transitions with considerable mixing of metal and ligand contributions (see Supporting Information Chapter 6). This finding is corroborated by UV/Vis-SEC results at the oxidation and reduction waves (Supporting Information Chapter 3.1).

Figure 4 summarizes the fs-TA experiments following excitation at 540 nm for all three heteroleptic Cu(I) complexes. After 300 fs a broad excited-state absorption (ESA) between 350 and 480 nm is accompanied by ground-state bleach (GSB) between 490 and 590 nm and a weaker ESA above 600 nm. In the first 10 ps the 400 nm ESA band apparently shifts red, due

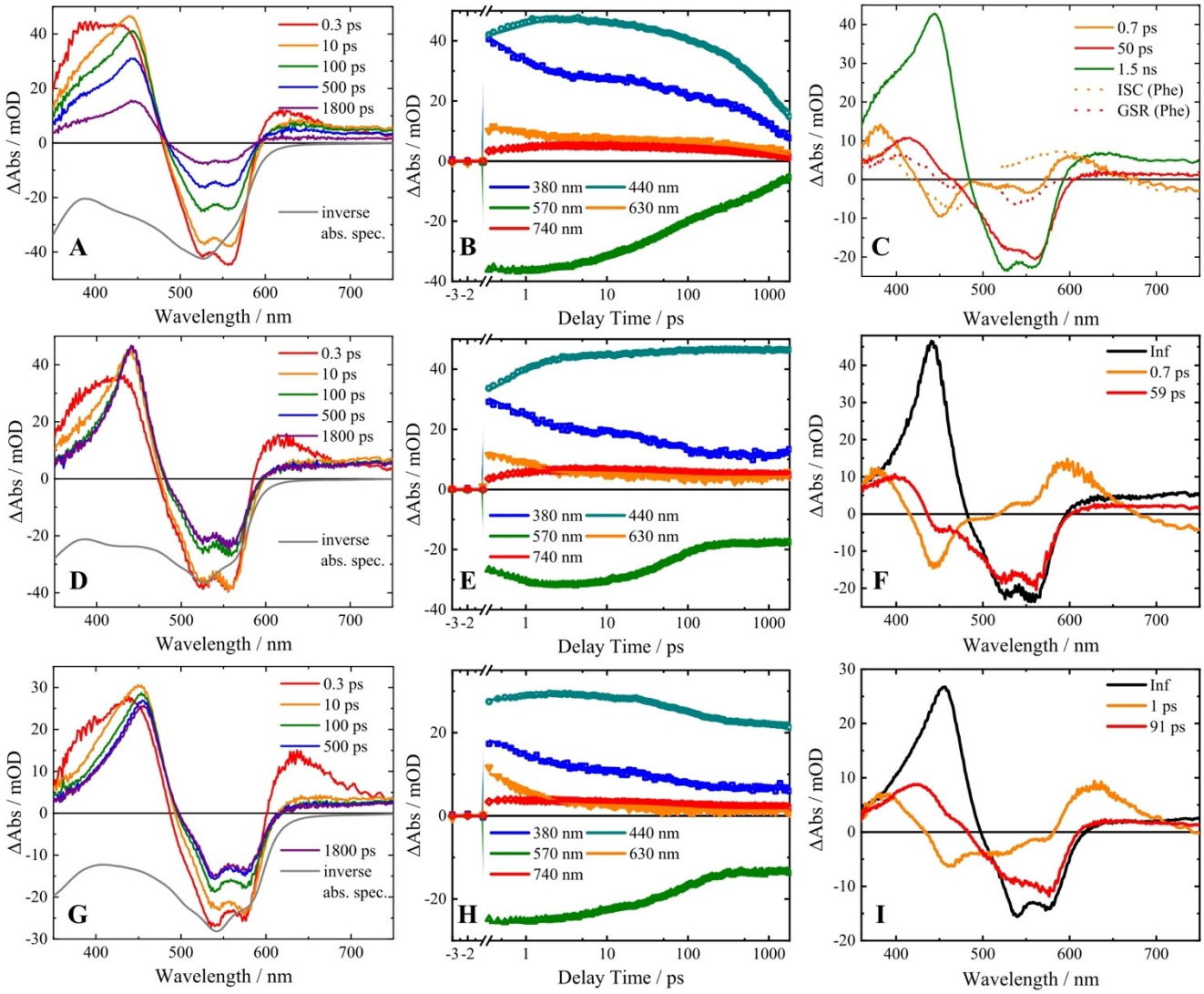

Figure 4. Temporal evolution of fs-TA spectra of **Cu–CF_3** (A), **Cu–F** (D), and **Cu–I** (G) upon pumping at 540 nm at different delay times dissolved in acetonitrile (including the inverted ground-state absorption spectrum as a gray line) is shown. Kinetic traces **Cu–CF_3** (B), **Cu–F** (E), and **Cu–I** (H) at selected probe wavelengths upon pumping at 540 nm. Decay-associated spectra (DAS) of **Cu–CF_3** (C), **Cu–F** (F), and **Cu–I** (I) upon pumping at 540 nm with three-(**Cu–CF_3**)/two-time constants (**Cu–F** and **Cu–I**) plus an infinite component received by the three-/two-exponential fit for analysis. In previously published literature on heteroleptic [Cu(xantphos)Im], named Phe similar processes are observed. Therefore, the dotted lines in the DAS of **Cu–CF_3** are shown as a comparison. The spectral features of the orange dotted line were correlated to an ISC while the spectral features of the red dotted line were assigned to a GSR for the complex Phe.[25]

to a decrease of the blue part around 350 nm and an increase of signal around 440 nm. On a similar timescale, a decay of the GSB and the ESA signal above 600 nm is observed. Within the experimentally accessible delay time window of the femtosecond TA experiment (~2 ns), the TA signal does not decay to zero (see Figure 4B) instead a long-lived signal component is observed.

The signal evolution can be described by three characteristic time constants (two time constants associated with exponential decay of the signal and one infinite component for **Cu**–**F** and **Cu**–**I** reflecting the long-lived signal component) and the related spectral changes are described by decay-associated spectra (DAS, see Figure 4C). The first time constant, $\tau_1 = 0.7$ ps, reflects a decreasing differential absorption at 380 and 600 nm and a signal increase at 450 and above 650 nm. Furthermore, an ESA decay at 600 nm and an increase of the differential absorption signal between 490 and 570 nm are associated with τ_1. The second time constant, $\tau_2 = 50$ ps, is related to a decreasing differential absorption at 415 nm and an increasing signal between 470 to 600 nm, that is, in the region of GSB. The third time constant is associated with the ground-state recovery from the lowest energy triplet state. For **Cu**–**CF$_3$** the third time constant, $\tau_3 = 1.5$ ns, reflects a broadly decaying differential absorption at 445 and above 600 nm as well as a recovery of the GSB from 480 to 600 nm. Although these spectral changes are correlated to the decay of the excited-state, the signal does not fully decay to zero in the observed time window. The temporal evolution of the excited-state population reflected by the infinite component was investigated by nanosecond time-resolved transient absorption, showing the decay of the excited-state population to the ground state (Figure 5, τ_3: 54 ns, **Cu**–**F**; Figure S28 τ_3: 31 ns **Cu**–**I**).

The spectral changes associated with τ_1 are reminiscent of the spectral signatures reported for short delay times for structurally-related heteroleptic [Cu(xantphos)Im] complexes (see dotted yellow line in Figure 4C).[25] In this previous investigation on the excited-state decay pathways of [Cu(xantphos)Im] complexes, we showed that after photoexcitation a large part of the excited-state population undergoes fast sub-picosecond ISC into the triplet manifold while the residual part undergoes pseudo-Jahn-Teller flattening (PJT) into two geometrically distinct, relaxed excited singlet states ($S_{1/2relax}$ or $S_{3/4relax}$; see below).[25] Our previous fs-TA data showed, that these relaxed singlet states are populated on an early picosecond time scale from either the S_1/S_2 or S_3/S_4 Franck-Condon states, respectively. Ground state recovery was only observed from the $S_{1/2relax}$ on a hundred picosecond time scale and internal conversion from $S_{3/4relax}$ to $S_{1/2relax}$ occurred on a similar time scale. The latter involves a geometrical reorientation of the xantphos ligand. Based on the striking similarity of the spectral signatures observed in this study with that previously reported by us[25], the first time constant τ_1 is assigned to rapid ISC in the triplet manifold. We assume that this process is occurring on a similar timescale as PJT in the excited singlet manifold, a process, which is however silent in the UV-Vis transient absorption data shown here.[25] The spectral changes associated with the second time constant, $\tau_2 = 50$–90 ps, also agree well with the previously made observations for [Cu(xantphos)Im] complexes (see dotted red line in Figure 4C).[25] Hence, we adopt the previously made assignment of the sub-100 ps processes to ground-state recovery (GSR) from the relaxed singlet manifold ($S_{1/2relax}$; see above). For [Cu(xantphos)Im] complexes the GSR process was observed on a time scale of 150 ps.[25] The shorter τ_2 for the title [Cu(PPh$_3$)$_2$Im] of about 50 ps (for **Cu**–**F** and **Cu**–**I**) is rationalized by the increased geometric flexibility of the PPh$_3$ ligand coordination geometry with respect to the more rigid xantphos ligand. Further evidence for the comparability of the excited-state decay pathways of the title complexes with [Cu(xantphos)Im] is given by the observations at 400 nm pump energy (see below).

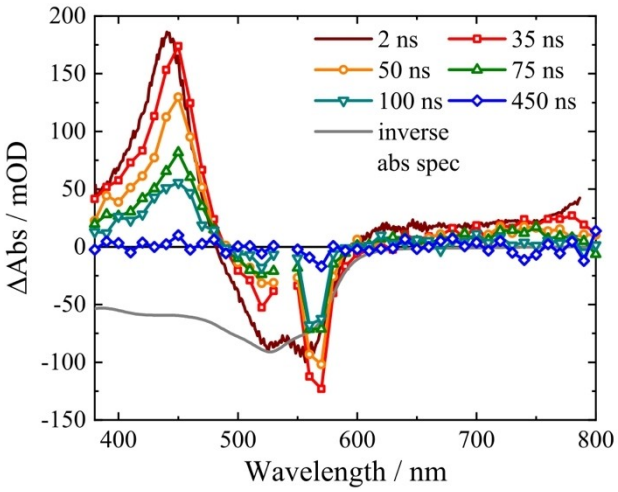

Figure 5. TA spectra of ns-TA experiments for **Cu**–**F** upon pumping at 540 nm.

Importantly, a planarization torsion of the *N*-aryl rings was previously observed for [Cu(xantphos)Im] complexes[25,31] on a 10 ps timescale. This torsional motion allows a delocalization of the excess charge over the imidazolate and *N*-aryl moieties and is mainly connected with an increasing ESA at about 450 nm. For the title complexes, this ESA is already present on sub-ps timescales and increases with the characteristic time constant τ_1. Likely, the geometric flexibility of the PPh$_3$ ligands allows for faster torsional reorganization. The decay, associated with the third time constant occurs from the energetically lowest triplet state, as evidenced by the spectral profile of the long-lived component, which resembles triplet state absorption as also observed for other heteroleptic Cu(I) complexes.[25,31] The above made interpretations are further supported with pump-wavelength dependent investigations. Figure 6 compares the fs-TA data for **Cu**–**CF$_3$** excited at 540 nm (excitation in S_1 and S_2; Figure 6A–C) and at 400 nm (excitation in S_3 and S_4; Figure 6D–F).For **Cu**–**F** and **Cu**–**I** the corresponding data are shown in the Supporting Information (Figure S31). The initial spectral behaviour of the fs-TA spectra is similar at both excitation wavelengths with an ESA band at 430 and above 600 nm as well as a GSB band at 500 nm. However, upon excitation at 540 nm, a more pronounced GSB is observed with two distinct minima at 530 and 570 nm. Excitation at 400 nm on the other hand leads

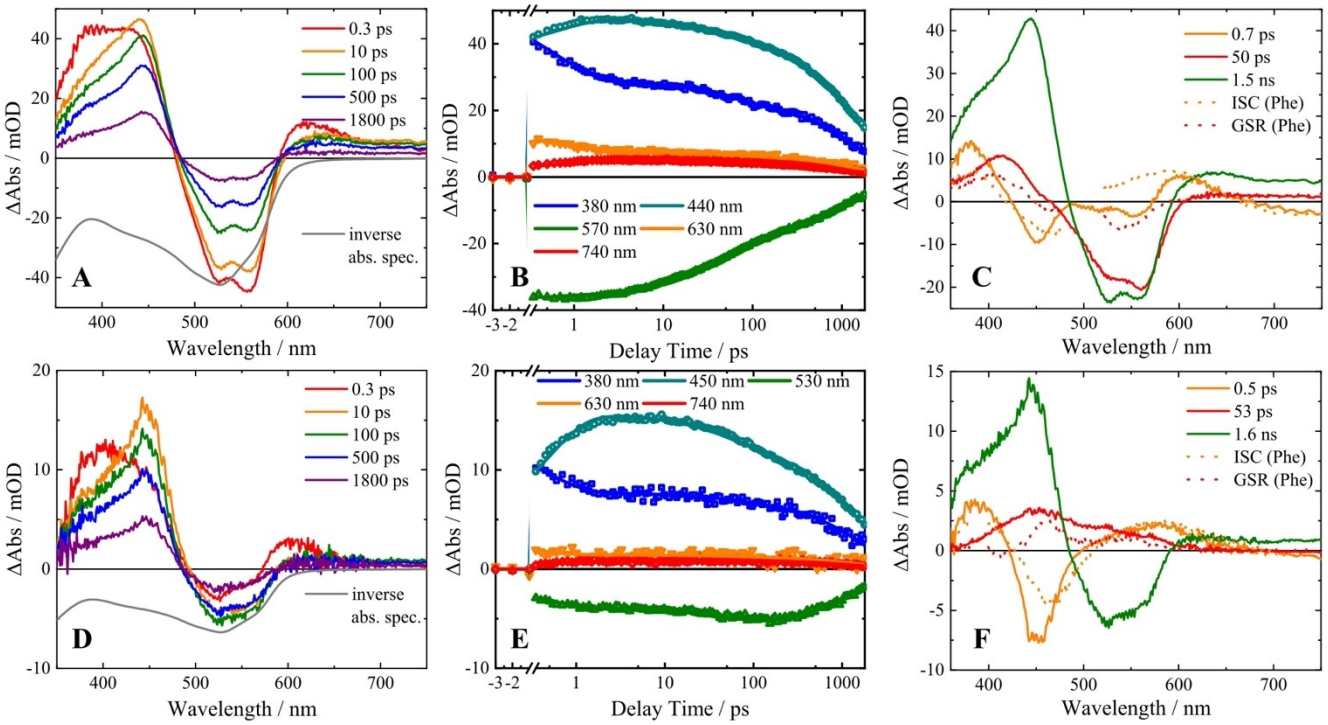

Figure 6. Comparison of fs-TA data by using excitation wavelengths of 540 (A–C) and 400 nm (D–F) of **Cu**–$\mathbf{CF_3}$ in acetonitrile at selected delay times (including the inverted ground-state absorption spectrum as a gray line). Kinetic traces at selected probe wavelengths and the decay-associated spectra (DAS) are given. For comparison, the DAS of the previously reported [Cu(xantphos)Im] (Phe) is shown as a dotted line. The orange dotted DAS was associated with an ISC/assumed PJT and the red dotted DAS was assigned to a GSR for complex Phe.[25]

to a single, non-structured GSB band. For the analysis of the fs-TA data upon excitation at 400 nm, a bi-exponential fit and an infinite component (**Cu**–**F**, **Cu**–**I**) or a triexponential fit (**Cu**–$\mathbf{CF_3}$) was necessary. The first time constant τ_1 ($\leq$1 ps) is associated with similar spectral features as observed at 540 nm excitation and likewise assigned to ISC and PJT flattening. However, the second time at 400 nm excitation shows a different spectral behavior compared to 540 nm. Here, a decay of the ESA between 400 to 600 nm is observed. In agreement with earlier made observations, we interpret this behavior as concomitantly occurring internal conversion (IC) from $S_{3/4relax}$ to $S_{1/2relax}$ and ground state recovery in the singlet manifolds.[25] The third time constant is again associated with the ground-state recovery from the lowest energy triplet state and was determined by ns-transient absorption spectroscopy (54 ns, **Cu**–**F**; 82 ns, **Cu**–**I**; Figure S27).

Figure 7 summarizes the experimental data on the excited-state relaxation of the investigated heteroleptic Cu(I) complexes in a single photophysical model: After photoexcitation at 400 and 540 nm ISC, as well as an assumed PJT, depopulate the Franck-Condon region yielding an ensemble of complexes partially populating a relaxed singlet excited-state and mainly the triplet manifold.

We associate this excited-state branching with the fact that the spin-orbit coupling in the complexes strongly depends on the geometry of the excited complex, that is, relaxation along the flattening coordinate (progressing PJT) reduces the spin-

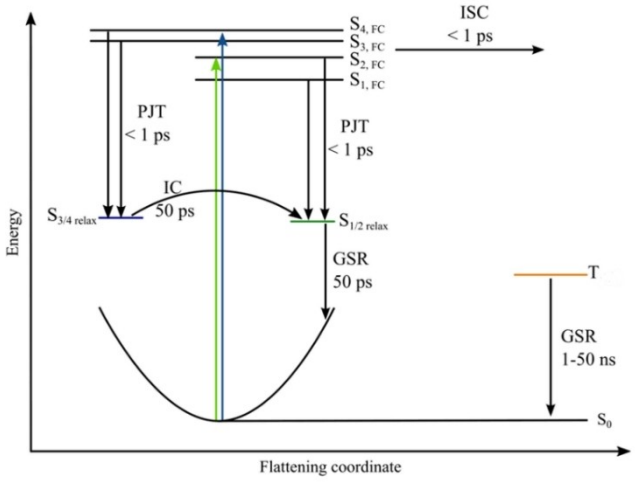

Figure 7. Simplified illustration of possible pathways occurring for the three heteroleptic Cu(I) complexes by pumping at 400 (blue arrow) and 540 nm (green arrow). After photoexcitation a fast intersystem crossing (ISC) and pseudo-Jahn-Teller (PJT) happen on a similar time scale of $\tau_1 \leq 1$ ps. After the ISC into the triplet manifold a ground-state recovery from the triplet into the singlet takes place ($\tau_3 = 1$ ns for **Cu**–$\mathbf{CF_3}$ and $\tau_3 = 30$–80 ns for **Cu**–**F** and **Cu**–**I**). On the singlet manifold, a relaxation of the singlet state takes place into $S_{1/2relax}$ after the occurring PJT. Then a ground-state recovery from the singlet state appears ($\tau_2 = 50$ ps). In the case of photoexcitation at 400 nm a competing process occurs for the ground-state recovery from the singlet state. Hereby, the relaxation after the appearing PJT occurs in the relaxed singlet states $S_{3/4relax}$. Then internal conversion ($\tau_2 = 50$ ps) into the relaxed $S_{1/2relax}$ states happens on a similar time scale as the ground-state recovery.

orbit coupling and hence competes efficiently with the population of the triplet state. The complexes populating the relaxed singlet state return to the electronic ground state on a sub-100 ps timescale, while ground-state recovery from the triplet manifold takes place on the ns timescale.

Conclusion

In this study, six new, neutral, heteroleptic Cu(I) 4*H*-imidazolate complexes are presented of which five bear monodentate PPh_3 co-ligands and one the bidentate xantphos ligand, the latter prepared as a reference. The substituent on the *N*-aryl of the $[Cu(PPh_3)_2Im]$ complexes was systematically varied to study their ground and excited-state properties in dependence on the substituent. The investigated $[Cu(PPh_3)_2Im]$ complexes engage in dynamic PPh_3 ligand exchange processes, which are unseen in the xantphos analogues. In contrast to the popular cationic $[Cu(PPh_3)_2(phenanthroline\text{-}type)]^+$ complexes, the formation of the respective homoleptic complexes is not observed. Moreover, the homoleptic $[Cu(Im)_2]^-$ complexes form $[Cu(PPh_3)_2(Im)]$ upon addition of PPh_3. This coordination behavior is attributed to the anionic nature of the Im^- ligand and the stronger binding of Cu(I) yet repulsive Im^-/Im^- interactions in the homoleptic complex.

All complexes show two 4*H*-imidazolate-based reductions, one Cu(I) based oxidation and one phosphorous-based oxidation process. The redox potentials reveal that $[Cu(PPh_3)_2(Im)]$ are easier to reduce yet harder to oxidize than its [Cu(xantphos)(Im)] congeners. As the latter complexes, also $[Cu(PPh_3)_2(Im)]$ possess broad and intense absorption features in the visible, owing to four charge transfer transitions. Excitation of these transitions is followed by a fast ISC to the triplet manifold for the major proportion of the exciting ensemble. The remaining minor singlet state population relaxes along the pseudo-Jahn–Teller flattening coordinate prior to ground state recovery on a ten picosecond time scale. Ground-state recovery from the excited triplet state takes place on a 2–50 ns timescale. Overall, the excited-state lifetime of $[Cu(PPh_3)_2(Im)]$ is shorter than for [Cu(xantphos)(Im)] complexes.

This is the first investigation of neutral $[Cu(PPh_3)_2Im]$ complexes, which offer a broad absorption spectrum, reversible reduction properties and sufficiently long excited state lifetimes to undergo photoreduction. The dynamic ligand exchange processes without the formation of the homoleptic complexes may open up photocatalytic reactions not accessible with the xantphos analogues.

Experimental Section

Chemicals: All synthetic manipulations were carried out under atmospheric conditions. Chemicals were purchased from Carl Roth (MeCN, DCM in spectroscopic grade for UV-vis-NIR experiments) and used without further purification, if not stated otherwise. Solvents for procedures under inert atmosphere were dried over sodium (THF) or calcium hydride (DCM, MeCN) and distilled under nitrogen atmosphere. To further remove oxygen three cycles of a freeze-pump-thaw (FPT) procedure were applied. Deuterated solvents were subjected to three FPT cycles and stored in a glovebox over mole sieve 3 Å. The basic anion exchange resin Amberlyst A21 was purchased from Alfa Aesar and was washed with DCM prior to use. The homoleptic cuprates, which were used in this work were prepared according to Ref. [39] and were used without further purification. *N*,*N*-dimethyltoluidine, $TBAPF_6$ (electrochemical grade), $TBABF_4$ (electrochemical grade) and PPh_3 were purchased from Sigma Aldrich.

NMR: Spectra (^1H, $^{13}C\{1H\}$, ^{31}P, ^{19}F) were recorded at 20 °C (if not stated otherwise) on Bruker Fourier (300 MHz), Avance III (400 MHz), Avance IV NEO (500 MHz) spectrometers. Chemical shifts are reported in parts per million relative to tetramethylsilane (^1H, $^{13}C\{^1H\}$ NMR), 85% phosphoric acid (^{31}P NMR) and trifluoromethane (^{19}F NMR) as external standards. The NMR signal was locked to the residual solvent signal. For NMR experiments under inert conditions, a NMR tube with a young valve (air-tight NMR tube) was used. Solutions were prepared and filled into the air-tight NMR tubes in a glovebox under nitrogen atmosphere or using standard Schlenk-technique.

ESI-MS: Measurements were carried out on a Bruker maXis instrument. The experimental isotope pattern ($[M^+]$) and the calculated isotope patterns were compared to ensure the identity of the substance.

UV-Vis-NIR absorption: Spectra are measured at room temperature on a Jasco V-780 spectrometer in 10 mm quartz cuvettes and are corrected for the solvent background.

CV experiments: Measurements were carried out at room temperature in a glove box using a three-electrode setup with glassy carbon as working electrode, a silver rod (∅ = 2 mm) as pseudo-reference and a platinum rod (∅ = 2 mm) as counter electrode. The ∅ = 3 mm glassy carbon electrodes were purchased from EDAQ, the silver rod (99.99%) and Pt rod (99.95%) were purchased from EcoChem. A VersaStat 3 potentiostat (Princeton Applied Research) was used for all the measurements, using the corresponding software VersaStudio 2.49.2.

UV-Vis-SEC: Measurements were performed in a 2 mm SEC cuvette under nitrogen atmosphere in the glovebox. The heteroleptic Cu(I) complexes (12 μM (**Cu**–**CF$_3$**), 26 μM (**Cu**–**F**), 13 μM (**Cu**–**I**)) were dissolved in anhydrous and degassed MeCN, containing 0.1 M $TBABF_4$ as supporting electrolyte. An ITO-coated PET film was used as a working electrode, together with a Pt wire as counter and Ag/AgCl pseudo-reference electrode. Before and after each measurement a cyclic voltammogram was recorded to ensure sample and electrode integrity. Potentials were applied with a VersaStat 3 potentiostat (Princeton Applied Research) using the corresponding software VersaStudio 2.49.2 and each run was started with the detection of the open circuit potential (OCP) for 30 s, followed by the respective potential for 5 min. Absorption changes induced at different potentials were collected with an AVANTES multichannel spectrometer and an AvaLight-DH-S-BAL (deuterium and halogen lamp) light source, fiber-coupled into the cuvette holder.

Fs-TA and ns-TA: Experiments were performed in a similar setup as described elsewhere.[25,31] For these experiments, the heteroleptic Cu(I) complexes were dissolved in anhdrous MeCN and measured in a 1 mm quartz cuvette with an optical density in the range of 0.3–0.5. The power of the pump pulse directly before the sample was 0.4 mW independent of the two pump wavelengths of 400 and 540 nm. To ensure reproducibility, UV-Vis spectra were recorded before and after the TA experiments.

Crystallographic data: The intensity data for the compounds were collected on a Nonius KappaCCD diffractometer using graphite-

monochromated $Mo_{K\alpha}$ radiation. Data were corrected for Lorentz and polarization effects; absorption was taken into account on a semi-empirical basis using multiple-scans.[41–44] The structures were solved by intrinsic phases (SHELXT[45]) and refined by full-matrix least squares techniques against F_o^2 (SHELXL-2014[46]). All hydrogen atoms were included at calculated positions with fixed thermal parameters. Disordered solvent molecule acetonitrile of **Cu–Cl** was refined using bond lengths restraints and displacement parameter restraints. Crystallographic data as well as structure solution and refinement details are summarized in Table S2. MERCURY[47] was used for structure representations.

Calculations: All calculations were performed using Gaussian 16 Rev.B.01.[48] The hybrid exchange correlation functional PBE0 in combination with the double-ζ basis set def2-SV(P)[49] and its corresponding electronic core potential was used for all calculations. All geometry optimizations were performed using Gaussian's tight threshold. To account for dispersion interactions, Grimme's D3 correction was applied in the Becke-Johnson damping version.[50] The solvent environment was included implicitly using the integral equation formalism variant of the polarizable continuum model (IEF-PCM)[51–53] for acetonitrile ($\varepsilon = 35.688$, $n = \varepsilon(\infty) = 1.806874$). Minimum geometries were verified to be local minima on the potential energy hypersurface by a normal mode analysis. Frequency and excitation calculations were performed without symmetry constraints using the optimized ground-state geometries. Within the TD-DFT calculations, the first 50 excited singlet transitions were taken into account. The percent contribution of the respective transitions were obtained using GaussSum 3.0[54] and charge density differences were analysed using the Multifwn tool[55,56] and are plotted at an isovalue = 0.0004.

General procedure for [Cu(PPh$_3$)$_2$Im] complexe preparation: In a Schlenk flask 0.576 g PPh_3 (2 equiv., 2.2 mmol) were mixed, at room temperature with 0.410 g $[Cu(MeCN)_4]PF_6$ (1 equiv., 1.1 mmol) in 10 mL MeCN until the PPh_3 was fully dissolved. In a separate flask 0.506 g 4*H*-imidazole (1 equiv., 1.1 mmol) were mixed with 1 g of Amberlyst A21 in 20 mL DCM. The solution was stirred at room temperature until a clear red coloration of the Amberlyst occurred. Both solutions were then combined and stirred at room temperature overnight or until the 4*H*-imidazole was fully dissolved. The Amberlyst was then filtered off and basic alumina was added to the filtrate, to remove unconsumed $[Cu(MeCN)_4]PF_6$. The solution was filtered again and left for crystallization (if not stated otherwise) by slow solvent diffusion. Alternatively, the crude solution was purified over basic alumina with 1:1 DCM/MeCN.

Synthesis of [Cu(xantphos)Im–CF$_3$]: In a Schlenk flask, 500 mg Im–CF_3 (1 equiv., 1.1 mmol) were mixed, at room temperature with 1 g Amberlyst A21 in 25 mL DCM. The DCM solution was stirred until no further coloration of the Amberlyst A21 was noticeable. In a separate flask, 406 mg $[Cu(MeCN)_4]PF_6$ (1 equiv., 1.1 mol) were mixed with 630 mg (9,9-dimethyl-9*H*-xanthene-4,5-diyl)bis(diphenylphosphane) (xantphos, 1 equiv., 1.1 mmol) in 5 mL MeCN and stirred at room temperature until everything was dissolved. Both solutions were then combined and stirred at room temperature overnight or until the 4*H*-imidazole was fully dissolved. The Amberlyst A21 was then filtered off and gel filtration on basic alumina with 1:1 DCM/MeCN was performed. After solvent removal, the residue was dissolved in toluene/MeCN 1:1.and left for crystallization. After a week red crystals could be obtained from the solution.

[(((3-Trifluormethane)phenyl)4-(3(trifluormethane)phenyl)imino-κN-2-phenyl-4*H*-imidazol-5-ylamido-κN)(triphenylphosphane-κP)$_2$Cu(I)] (**Cu–CF$_3$**). Red crystals were obtained from a 1:1 MeCN/toluene solution by slow solvent diffusion. Yield: 33% (0.379 g). ^{1}H NMR (CD_2Cl_2, 500 MHz) δ/ppm: 8.39 (br d, J = 7.6 Hz, 2H, $^{o-CH}$2-Ph), 7.57 (t, J = 7.3 Hz, 1H, $^{p-CH}$2-Ph), 7.47 (t, J = 7.9 Hz, 2H, $^{m-CH}$2-Ph), 7.43 (br s, 2H, $^{C2H}N^{Ar}$), 7.32 (t, J = 7.3 Hz, 6H; $^{p-CH}$PPh), 7.27 (br d, J = 7.9 Hz, 2H, $^{C4H}N^{Ar}$), 7.24 (br d, J = 8.2 Hz, 2H, $^{C6H}N^{Ar}$), 7.10–7.18 (m, 14H; $^{m-CH}$PPh/$^{C6H}N^{Ar}$), 7.02–7.08 (m, 12H; $^{o-CH}$PPh). ^{13}C NMR (CD_2Cl_2, 151 MHz) δ/ppm: 194.2 ($^{ipso-C2}$Im^{core}), 172.4 (^{C4,C5}Im^{core}), 149.1 ($^{ipso-C}N^{Ar}$), 134.4 ($^{o-CH}$2-Ph), 133.9 ($^{o-CH}$PPh), 133.0 ($^1J_{C,P}$ = 21.9 Hz, $^{ipso-C}$PPh), 130.9 ($^2J_{C,F}$ = 31.9 Hz, $^{C3-CF3}N^{Ar}$), 130.4 ($^{p-CH}$PPh), 130.3 ($^{o-CH}$2-Ph), 129.6 ($^{C6H}N^{Ar}$), 129.3 ($^{C5H}N^{Ar}$), 129.2 ($^{m-CH}$PPh), 128.8 ($^{m-CH}$2-Ph), 125.1 ($^1J_{C,F}$ = 272.3 Hz, $^{CF3-C3}N^{Ar}$), 122.5 ($^3J_{C,F}$ = 4.0 Hz, $^{C2H}N^{Ar}$), 121.4 ($^3J_{C,F}$ = 4.0 Hz, $^{C4H}N^{Ar}$). ^{19}F NMR (CD_2Cl_2, 377 MHz) δ/ppm: −62.7. ^{31}P NMR (CD_2Cl_2, 162 MHz) δ/ppm: 0.16. MS (ESI pos): m/z (%) = 1047 $[MH]^+$, 587 $[Cu(PPh_3)_2]^+$ (100). Elemental analysis: calc. C 67.65, H 4.14, N 5.35%, found (+ 1/6 toluene) C 67.99, H 4.20, N 5.27%.

[((4-Fluorophenyl)(4-(4-fluorophenyl)imino-κN)-2-phenyl-4*H*-imidazol-5-ylamido-κN)(triphenylphosphane-κP)$_2$Cu(I)] (**Cu–F**). Red crystals. Yield: 36% (0.107 g). ^{1}H NMR (CD_2Cl_2, 300 MHz) δ/ppm:8.41 (br d, $^3J_{H,H}$ = 6.9 Hz, 2H, $^{o-CH}$2-Ph), 7.56 (t, $^3J_{H,H}$ = 7.2 Hz, 1H, $^{p-CH}$2-Ph), 7.47 (t, J = 6.9 Hz, 2H, $^{m-CH}$2-Ph), 7.35 (tt, $^3J_{H,H}$ = 7.3, 1.2 Hz, 6H, $^{p-CH}$PPh), 7.04–7.22 (m, 16H, $^{m-CH}$PPh, $^{o-CH}$2-Ph, $^{o-CH}N^{Ar}$), 7.04–7.22 (m, 16H, $^{m-CH}$PPh, $^{o-CH}N^{Ar}$), 7.02–7.12 (m, 12H, $^{o-CH}$PPh) 6.70 (br t, $^3J_{H,H}$ = 8.7 Hz, 4H, $^{m-CH}N^{Ar}$). ^{13}C NMR (CD_2Cl_2, 151 MHz) δ/ppm: 191.8 ($^{ipso-C2}$Im^{core}), 171.5 (^{C4,C5}Im^{core}), 160.3 ($^1J_{C,F}$ = 272.3 Hz, $^{CF}N^{Ar}$), 144.7 ($^{ipso-C}N^{Ar}$), 134.8 ($^{ipso-C}$2-Ph), 134.0 ($^2J_{C,P}$ = 10.4 Hz, $^{o-CH}$PPh), 133.4 ($^1J_{C,P}$ = 26.0 Hz, $^{ipso-C}$PPh), 132.7 ($^{p-CH}$2-Ph), 130.3 ($^{p-CH}$2-Ph), 130.1 ($^{o-CH}$2-Ph), 129.1 ($^{m-CH}$PPh), 128.7 ($^{m-CH}$2-Ph), 127.7 ($^3J_{C,F}$ = 7.8 Hz, $^{o-CH}N^{Ar}$), 115.1 ($^2J_{C,F}$ = 22.1 Hz, $^{m-CH}N^{Ar}$). ^{19}F NMR (CD_2Cl_2, 377 MHz) δ/ppm: −119.1. ^{31}P NMR (CD_2Cl_2, 162 MHz) δ/ppm: −0.36. MS (ESI): m/z (%) = 947 $[MH]^+$, 587 $[Cu(PPh_3)_2]^+$ (100). Elemental analysis: calc. C 70.91, H 4.70, N 5.80% (+1 H_2O), found C 71.13, H 4.64, N 6.12%.

[((4-Chlorophenyl)(4-(4-chlorophenyl)imino-κN)-2-phenyl-4*H*-imidazol-5-ylamido-κN)(triphenylphosphane-κP)$_2$Cu(I)] (**Cu-Cl**). Red crystals. Yield: 64% (0.185 g). ^{1}H NMR (CD_2Cl_2, 400 MHz) δ/ppm: 8.41 (br d, J = 7.3 Hz, 2H, $^{o-CH}$2-Ph), 7.56 (t, J = 7.3 Hz, 1H, $^{p-CH}$2-Ph), 7.47 (t, J = 7.3 Hz, 2H, $^{m-CH}$2-Ph), 7.35 (t, J = 7.3 Hz, 6H, $^{p-CH}$PPh), 7.20 (t, J = 7.6 Hz, 16H, $^{m-CH}$PPh, $^{o-CH}N^{Ar}$), 7.02-7.10 (m, 12H, $^{o-CH}$PPh), 6.96 (br d, J = 8.5 Hz, 4H, $^{m-CH}N^{Ar}$). ^{13}C NMR (CD_2Cl_2, 151 MHz) δ/ppm:193.23 (^{C2}Im), 171.7 ($^{C4/5}$Im), 147.1 ($^{ipso-C}N^{Ar}$), 134.0 (d, $^2J_{C,P}$ = 9.1 Hz, $^{o-CH}$PPh), 133.3 (d, $^1J_{C,P}$ = 24.7 Hz, $^{ipso-C}$PPh), 132.9 ($^{p-CH}$2-Ph), 132.4 ($^{ipso-C}$2-Ph), 130.4 ($^{p-CH}$PPh), 130.2 ($^{o-CH}$2-Ph), 129.8 ($^{CCl}N^{Ar}$), 129.2 ($^{m-CH}$PPh), 128.7 ($^{o-CH}$PPh), 128.6 ($^{m-CH}N^{Ar}$), 127.6 ($^{o-CH}N^{Ar}$). ^{31}P NMR (CD_2Cl_2, 162 MHz): δ = −0.16 ppm. MS (ESI): m/z (%) = 979 $[MH^+]$, 578 $[Cu(PPh_3)_2]^+$ (100). Elemental analysis: calc. C 69.20, H 4.48, N 5.66% (+1/2H_2O), found C 69.31, H 4.41, N 5.81%.

[((4-Bromophenyl)(4-(4-bromophenyl)imino-κN)-2-phenyl-4*H*-imidazol-5-ylamido-κN)(triphenylphosphane-κP)$_2$Cu(I)] (**Cu–Br**). Violet crystals. Yield: 39% (0.118 g). ^{1}H NMR (CD_2Cl_2, 300 MHz) δ/ppm: 8.41 (br d, J = 7.0 Hz, 2H, $^{o-CH}$2-Ph), 7.57 (t, J = 7.3 Hz, 1H, $^{p-CH}$2-Ph), 7.47 (t, J = 7.2 Hz, 2H, $^{m-CH}$2-Ph), 7.36 (t, J = 7.4 Hz, 6H, $^{p-CH}$PPh), 7.00-7.24 ppm (m, 32H, $^{m-CH}$PPh, $^{o-CH}$PPh, $^{o-CH}N^{Ar}$, $^{m-CH}N^{Ar}$). ^{13}C NMR (CD_2Cl_2, 151 MHz): 193.1 (^{C2}Im^{core}), 171.4 (^{C4,C5}Im^{core}), 147.5 ($^{ipso-C}N^{Ar}$), 134.1 (d, $^2J_{C,P}$ = 11.7 Hz,$^{o-CH}$PPh), 133.3 (d, $^1J_{C,P}$ = 27.3 Hz, $^{ipso-C}$PPh), 132.8 ($^{p-CH}$2-Ph), 132.4 ($^{ipso-C}$2-Ph), 131.6 ($^{o-CH}N^{Ar}$), 130.4 ($^{p-CH}$PPh), 130.2 ($^{o-CH}$2-Ph), 129.2 ($^{m-CH}$PPh), 128.7 ($^{m-CH}$2-Ph), 127.9 ($^{o-CH}N^{Ar}$), 118.0 ppm ($^{CBr}N^{Ar}$). ^{31}P NMR (CD_2Cl_2, 162 MHz) δ/ppm: −1.85. MS (ESI): m/z (%) = 1067 $[MH^+]$, 578 $[Cu(PPh_3)_2]^+$ (100). Elemental analysis: calc. C 63.49, H 4.11, N 5.20% (+1/2 H2O), found C 63.55, H 3.97, N 5.35%.

[((4-Iodophenyl)(4-(4-iodophenyl)imino-κN)-2-phenyl-4*H*-imidazol-5-ylamido-κN)(triphenylphosphane-κP)$_2$Cu(I)] (**Cu–I**). Violet crystals. Yield: 37% (0.100 g). ^{1}H NMR (CD_2Cl_2, 500 MHz) δ/ppm: 8. 41 (d, 2H; J = 7.2 Hz, $^{o-CH}$2-Ph); 7.56 (t, 1H, J = 7.3 Hz; $^{p-CH}$2-Ph), 7.47 (t, 2H, J = 7.5 Hz, $^{m-CH}$2-Ph), 7.35 (t, 6H, J = 7.4 Hz, $^{p-CH}$PPh), 7.31 (d, 4H, J =

8.0 Hz, $^{o-CH}N^{Ar}$), 7.16 (t, 12H, J = 7.7 Hz, $^{m-CH}$PPh), 7.06 (m, 12H, $^{o-CH}$PPh), 6.93 (d, 4H, J = 6.1 Hz, $^{m-CH}N^{Ar}$). ^{13}C NMR (CD_2Cl_2, 151 MHz) δ/ppm: 193.3 ($^{C2}Im^{core}$), 171.7 ($^{C4,C5}Im^{core}$), 148.2 ($^{ipso-C}N^{Ar}$), 137.7 ($^{o-CH}N^{Ar}$), 134.0 (d, $^{2}J_{C,P}$ = 5.0 Hz, $^{o-CH}$PPh), 133.3 (d, $^{1}J_{C,P}$ = 24.9 Hz, $^{ipso-C}$PPh), 132.9 ($^{p-CH}$2-Ph), 132.5 ($^{ipso-CH}$2-Ph), 130.4 ($^{p-CH}$PPh), 130.2 ($^{o-CH}$PPh), 129.2 ($^{m-CH}$PPh), 128.7 ($^{m-CH}$2-Ph), 128.3 ($^{o-CH}N^{Ar}$), 88.9 ($^{Cl}N^{Ar}$). ^{31}P NMR (CD_2Cl_2, 162 MHz) δ/ppm: −0.10. MS (ESI): m/z (%) = 1163 [MH^+], 578 [$Cu(PPh_3)_2]^+$ (100). Elemental analysis: calc. C 58.85, H 3.73, N 4.82%, found C 58.66, H 3.73, N 5.13%.

[(((3-Trifluormethane)phenyl)4-(3(trifluormethane)phenyl)iminoκN-2-phenyl-4*H*-imidazol-5-ylamido-κN)((9,9-dimethyl-9H-xanthene-4,5-diyl)bis(diphenyl-phosphane))) Cu(I)] **[Cu(xantphos)Im−CF_3]** Red crystals. Yield: 28% (0.246 g). ^{1}H NMR (CD_2Cl_2, 400 MHz) δ/ppm: 8.38 (d, 2H, $^{o-CH}$2-Ph), 7.74 (s, 1H, $^{C2H}N^{Ar}$), 7.56 (t, ^{3}J = 7.3 Hz, 1H, $^{p-CH}$2-Ph), 7.51 (br dd, ^{3}J = 7.60 Hz, ^{3}J = 1.1 Hz, 2H, ^{C1H,C8H}xanthene), 7.46 (t, ^{3}J = 7.3 Hz, 2H, $^{m-CH}$2-Ph), 7.26 (t, 4H, ^{3}J = 7.0 Hz, $^{p-CH}$PPh), 7.03–7.17 (m, 20H, $^{C4H}N^{Ar}$, ^{C2H,C7H}xanthene, $^{o,m-CH}$PPh), 6.92 (d, ^{3}J = 7.6 Hz, 2H, $^{C6H}N^{Ar}$), 6.86 (t, 2 H, ^{3}J = 7.6 Hz, $^{C5H}N^{Ar}$), 6.51–6.56 (m, 2H, ^{C3H,C7H}xanthene), 1.64 (s, 6 H, $^{CH3-C9}$xanthene). ^{13}C NMR (CD_2Cl_2, 101 MHz) δ/ppm: 193.56 ($^{C2}Im^{core}$), 171.97 ($^{C4,C5}Im^{core}$), 155.45 (t, $^{2}J_{C,P}$ = 6.1 Hz, ^{C4a,C5a}xanthene), 149.21 ($^{C1}N^{Ar}$), 134.43 ($^{ipso-C}$2-Ph), 134.25 (^{C9a,C10a}xanthene), 133.71 (m, $^{o-CH}$PPh, $^{2}J_{C,P}$ = 8.7 Hz), 133.08 ($^{p-CH}$2-Ph), 132.56 (m, $^{1}J_{C,P}$ = 16.5 Hz, $^{ipso-C}$PPh), 131.04 (^{C3H,C7H}xanthene), 130.76 (q, $^{2}J_{C,F}$ = 32.08 Hz, $^{C-CF3}N^{Ar}$), 130.26 ($^{o-CH}$2-Ph), 130.21 ($^{p-CH}$PPh), 129.1 ($^{C6H}N^{Ar}$),129.09 ($^{m-CH}$PPh) 129.04 ($^{C5H}N^{Ar}$), 128.76 ($^{m-CH}$2-Ph), 127.02 (^{C1H,C9H}xanthene), 125.35 (^{C2H,C8H}xanthene), 124.37 (q, $^{1}J_{C,F}$ = 272.2 Hz, $^{CF3}N^{Ar}$), 121.75 (q, $^{3}J_{C,F}$ = 3.5 Hz, $^{p-CH}$PPh), 121.33 (^{C4H,C6H}xanthene), 121.07 (q, $^{3}J_{C,F}$ = 3.5 Hz, $^{4-CH}N^{Ar}$), 36.46 (^{C10}xanthene), 27.99 ($^{CH3-C10}$xanthene). ^{19}F NMR (CD_2Cl_2, 377 MHz) δ/ppm: -62.46. ^{31}P NMR (CD_2Cl_2, 162 MHz) δ/ppm: −13.26. MS (ESI): m/z (%) = 1101 $[MH]^+$ (1), 641 $[Cu(xantphos)]^+$ (100). Elemental analysis: calc. C 68.65, H 4.14, N 5.35% (+1/2 toluene, +1/2 MeCN) found C 68.38, H 4.36, N 5.40%.

Supporting Information

Deposition Number(s) 2212908 for **[Cu(xant)Im−CF_3]**, 2212909 for **Cu−CF_3**, and 2212910 for **Cu−Cl** contain(s) the supplementary crystallographic data for this paper. These data are provided free of charge by the joint Cambridge Crystallographic Data Centre and Fachinformationszentrum Karlsruhe Access Structures service.

Details for synthesis and structural characterization, single-crystal-X-Ray structural analysis, UV-Vis-spectroscopy, cyclic voltammetry, transient absorption spectroscopy data, and theoretical calculation details.

Acknowledgements

The authors gratefully acknowledge support by the Deutsche Forschungsgemeinschaft (DFG, German Research Foundation) - Projektnummer 364549901-TRR 234 "CataLight". Financial support by the Ernst-Abbe-Stiftung Jena for the ACD/Labs Spectrus processor license, which was used for NMR analysis is gratefully acknowledged. The authors thank the NMR platform at the Friedrich Schiller University Jena for carrying out the NMR experiments and particularly Dr. Peter Bellstedt for the installation of the *in situ* illumination NMR setup. Open Access funding enabled and organized by Projekt DEAL.

Conflict of Interest

The authors declare no competing financial interest.

Data Availability Statement

The data that support the findings of this study are available in the Supporting material of this article.

Keywords: copper · 4*H*-imidazolate ligands · ligand exchange reaction, phosphine ligands, transient absorptions spectroscopy

[1] P. A. Forero Cortés, M. Marx, M. Trose, M. Beller, *Chem Catal.* **2021**, *1*, 298–338.
[2] F. Doettinger, Y. Yang, M. A. Schmid, W. Frey, M. Karnahl, S. Tschierlei, *Inorg. Chem.* **2021**, *60*, 5391–5401.
[3] C. Sandoval-Pauker, G. Molina-Aguirre, B. Pinter, *Polyhedron* **2021**, *199*, 115105.
[4] E. Mejía, S.-P. Luo, M. Karnahl, A. Friedrich, S. Tschierlei, A.-E. Surkus, H. Junge, S. Gladiali, S. Lochbrunner, M. Beller, *Chem. Eur. J.* **2013**, *19*, 15972–15978.
[5] M. A. Schmid, M. Rentschler, W. Frey, S. Tschierlei, M. Karnahl, *Inorganics* **2018**, *6*, 134.
[6] M. Heberle, S. Tschierlei, N. Rockstroh, M. Ringenberg, W. Frey, H. Junge, M. Beller, S. Lochbrunner, M. Karnahl, *Chem. Eur. J.* **2017**, *23*, 312–319.
[7] M. Karnahl, E. Mejía, N. Rockstroh, S. Tschierlei, S. P. Luo, K. Grabow, A. Kruth, V. Brüser, H. Junge, S. Lochbrunner, M. Beller, *ChemCatChem* **2014**, *6*, 82–86.
[8] Y. Zhang, L. Zedler, M. Karnahl, B. Dietzek, *Phys. Chem. Chem. Phys.* **2019**, *21*, 10716–10725.
[9] S. Styring, *Faraday Discuss.* **2012**, *155*, 357–376.
[10] S. Tschierlei, M. Karnahl, N. Rockstroh, H. Junge, M. Beller, S. Lochbrunner, *ChemPhysChem* **2014**, *15*, 3709–3713.
[11] Y. Zhang, P. Traber, L. Zedler, S. Kupfer, S. Gräfe, M. Schulz, W. Frey, M. Karnahl, B. Dietzek, *Phys. Chem. Chem. Phys.* **2018**, *20*, 24843–24857.
[12] Y. Zhang, M. Schulz, M. Wächtler, M. Karnahl, B. Dietzek, *Coord. Chem. Rev.* **2018**, *356*, 127–146.
[13] L. Pathaw, D. Maheshwaran, T. Nagendraraj, T. Khamrang, M. Velusamy, R. Mayilmurugan, *Inorg. Chim. Acta* **2021**, *514*, 119999.
[14] D. G. Cuttell, S.-M. M. Kuang, P. E. Fanwick, D. R. McMillin, R. A. Walton, *J. Am. Chem. Soc.* **2002**, *124*, 6–7.
[15] C. E. A. Palmer, D. R. McMillin, *Inorg. Chem.* **1987**, *26*, 3837–3840.
[16] J. R. Kirchhoff, W. R. Robinson, D. R. Powell, A. T. Mckenzie, S. Chen, D. R. Mcmillin, *Inorg. Chem.* **1985**, *24*, 3928–3933.
[17] R. A. Rader, D. R. McMillin, M. T. Buckner, T. G. Matthews, D. J. Casadonte, R. K. Lengel, S. B. Whittaker, L. M. Darmon, F. E. Lytle, *J. Am. Chem. Soc.* **1981**, *103*, 5906–5912.
[18] M. Holler, B. Delavaux-Nicot, J. Nierengarten, *Chem. Eur. J.* **2019**, *25*, 4543–4550.
[19] D. Kakizoe, M. Nishikawa, Y. Fujii, T. Tsubomura, *Dalton Trans.* **2017**, *46*, 14804–14811.
[20] S. Tschierlei, M. Karnahl, M. Presselt, B. Dietzek, J. Guthmuller, L. González, M. Schmitt, S. Rau, J. Popp, *Angew. Chem. Int. Ed.* **2010**, *49*, 3981–3984; *Angew. Chem.* **2010**, *122*, 4073–4076.
[21] W. Villarreal, L. Colina-Vegas, G. Visbal, O. Corona, R. S. Corrêa, J. Ellena, M. R. Cominetti, A. A. Batista, M. Navarro, *Inorg. Chem.* **2017**, *56*, 3781–3793.
[22] L. J. Goossen, N. Rodríguez, B. Melzer, C. Linder, G. Deng, L. M. Levy, *J. Am. Chem. Soc.* **2007**, *129*, 4824–4833.
[23] L. J. Gooßen, N. Rodríguez, F. Manjolinho, P. P. Lange, *Adv. Synth. Catal.* **2010**, *352*, 2913–2917.
[24] M. Schulz, N. Hagmeyer, F. Wehmeyer, G. Lowe, M. Rosenkranz, B. Seidler, A. Popov, C. Streb, J. G. Vos, B. Dietzek, *J. Am. Chem. Soc.* **2020**, *142*, 15722–15728.
[25] B. Seidler, M. Sittig, C. Zens, J. H. Tran, C. Müller, Y. Zhang, K. R. A. A. Schneider, H. Görls, A. Schubert, S. Gräfe, M. Schulz, B. Dietzek, *J. Phys. Chem. B* **2021**, *125*, 11498–11511.
[26] M. Schulz, F. Dröge, F. Herrmann-Westendorf, J. Schindler, H. Görls, M. Presselt, *Dalton Trans.* **2016**, *45*, 4835–4842.

[27] C. Müller, M. Schulz, M. Obst, L. Zedler, S. Gräfe, S. Kupfer, B. Dietzek, *J. Phys. Chem. A* **2020**, *124*, 6607–6616.
[28] S. Amthor, S. Knoll, M. Heiland, L. Zedler, C. Li, D. Nauroozi, W. Tobaschus, A. K. Mengele, M. Anjass, U. S. Schubert, B. Dietzek-Ivanšić, S. Rau, C. Streb, *Nat. Chem.* **2022**, *14*, 321–327.
[29] Y. Zhang, M. Heberle, M. Wächtler, M. Karnahl, B. Dietzek, M. Waechtler, M. Karnahl, B. Dietzek, *RSC Adv.* **2016**, *6*, 105801–105805.
[30] G. Bowmaker, P. Healy, L. Engelhardt, J. Kildea, B. Skelton, A. White, *Aust. J. Chem.* **1990**, *43*, 1697.
[31] M. Schulz, C. Reichardt, C. Müller, K. R. A. Schneider, J. Holste, B. Dietzek, *Inorg. Chem.* **2017**, *56*, 12978–12986.
[32] L. Koefoed, S. U. Pedersen, K. Daasbjerg, *Langmuir* **2017**, *33*, 3217–3222.
[33] N. A. Gothard, M. W. Mara, J. Huang, J. M. Szarko, B. Rolczynski, J. V. Lockard, L. X. Chen, *J. Phys. Chem. A* **2012**, *116*, 1984–1992.
[34] M. W. Mara, N. E. Jackson, J. Huang, A. B. Stickrath, X. Zhang, N. A. Gothard, M. A. Ratner, L. X. Chen, *J. Phys. Chem. B* **2013**, *117*, 1921–1931.
[35] Z. A. Siddique, Y. Yamamoto, T. Ohno, K. Nozaki, *Inorg. Chem.* **2003**, *42*, 6366–6378.
[36] V. Leandri, A. R. P. Pizzichetti, B. Xu, D. Franchi, W. Zhang, I. Benesperi, M. Freitag, L. Sun, L. Kloo, J. M. Gardner, *Inorg. Chem.* **2019**, *58*, 12167–12177.
[37] M. Iwamura, S. Takeuchi, T. Tahara, *Acc. Chem. Res.* **2015**, *48*, 782–791.
[38] S. Garakyaraghi, E. O. Danilov, C. E. McCusker, F. N. Castellano, *J. Phys. Chem. A* **2015**, *119*, 3181–3193.
[39] J. H. Tran, P. Traber, B. Seidler, H. Görls, S. Gräfe, M. Schulz, *Chem. Eur. J.* **2022**, *28*, e202200121.
[40] C. L. Linfoot, P. Richardson, T. E. Hewat, O. Moudam, M. M. Forde, A. Collins, F. White, N. Robertson, *Dalton Trans.* **2010**, *39*, 8945–56.
[41] B. Hooft, R. Nonius, *BV Nonius*, Delft, Netherlands **1998**.
[42] Z. Otwinowski, W. Minor in Methods Enzymology, Vol. 276: Macromolecular Crystallography, Part A (Eds.: C. W. Carter, R. M. Sweet), Academic Press, 1997, pp. 307–326.
[43] L. Krause, R. Herbst-Irmer, G. M. Sheldrick, D. Stalke, *J. Appl. Crystallogr.* **2015**, *48*, 3–10.
[44] S. Sheldrick, SADABS 2.10, Madison WI, 2002.
[45] G. M. Sheldrick, *Acta Crystallogr. Sect. A* **2015**, *71*, 3–8.
[46] G. M. Sheldrick, *Acta Crystallogr. Sect. C* **2015**, *71*, 3–8.
[47] C. F. Macrae, P. R. Edgington, P. McCabe, E. Pidcock, G. P. Shields, R. Taylor, M. Towler, J. van de Streek, *J. Appl. Crystallogr.* **2006**, *39*, 453–457.
[48] M. J. Frisch, G. W. Trucks, H. B. Schlegel, G. E. Scuseria, M. A. Robb, J. R. Cheeseman, G. Scalmani, V. Barone, G. A. Petersson, H. Nakatsuji, X. Li, M. Caricato, A. V. Marenich, J. Bloino, B. G. Janesko, R. Gomperts, B. Mennucci, H. P. Hratchian, J. V. Ortiz, A. F. Izmaylov, J. L. Sonnenberg, Williams, F. Ding, F. Lipparini, F. Egidi, J. Goings, B. Peng, A. Petrone, T. Henderson, D. Ranasinghe, V. G. Zakrzewski, J. Gao, N. Rega, G. Zheng, W. Liang, M. Hada, M. Ehara, K. Toyota, R. Fukuda, J. Hasegawa, M. Ishida, T. Nakajima, Y. Honda, O. Kitao, H. Nakai, T. Vreven, K. Throssell, J. A. Montgomery Jr., J. E. Peralta, F. Ogliaro, M. J. Bearpark, J. J. Heyd, E. N. Brothers, K. N. Kudin, V. N. Staroverov, T. A. Keith, R. Kobayashi, J. Normand, K. Raghavachari, A. P. Rendell, J. C. Burant, S. S. Iyengar, J. Tomasi, M. Cossi, J. M. Millam, M. Klene, C. Adamo, R. Cammi, J. W. Ochterski, R. L. Martin, K. Morokuma, O. Farkas, J. B. Foresman, D. J. Fox, **2016**, Gaussian 16, Revision C.01, Gaussian, Inc., Wallin.
[49] C. Adamo, V. Barone, *J. Chem. Phys.* **1999**, *110*, 6158–6170.
[50] S. Grimme, S. Ehrlich, L. Goerigk, *J. Comput. Chem.* **2011**, *32*, 1456–1465.
[51] E. Cancès, B. Mennucci, J. Tomasi, *J. Chem. Phys.* **1997**, *107*, 3032–3041.
[52] E. Cancès, B. Mennucci, *J. Math. Chem.* **1998**, *23*, 309–326.
[53] J. Tomasi, B. Mennucci, R. Cammi, *Chem. Rev.* **2005**, *105*, 2999–3094.
[54] N. M. O'Boyle, A. L. Tenderholt, K. M. Langner, *J. Comput. Chem.* **2008**, *29*, 839–845.
[55] T. Lu, F. Chen, *J. Comput. Chem.* **2012**, *33*, 580–592.
[56] Z. Liu, T. Lu, Q. Chen, *Carbon* **2020**, *165*, 461–467.

Manuscript received: October 18, 2022
Accepted manuscript online: February 22, 2023
Version of record online: March 27, 2023